4-30-2012

Absolute Properties of the Eclipsing Binary Star BF Draconis

Claud H. Sandberg Lacy
University of Arkansas, Fayetteville

Guillermo Torres
Harvard-Smithsonian Center for Astrophysics

Francis C. Fekel
Tennessee State University

Jeffrey A. Sabby
Southern Illinois University Edwardsville

Antonio Claret
Instituto de Astrofisica de Andalucia

Recommended Citation

Claud H. Sandberg Lacy et al 2012 AJ 143 129

The Astronomical Journal, 143:129 (18pp), 2012 June doi:10.1088/0004-6256/143/6/129

ABSOLUTE PROPERTIES OF THE ECLIPSING BINARY STAR BF DRACONIS

Claud H. Sandberg Lacy[1,6], Guillermo Torres[2], Francis C. Fekel[3,6,7], Jeffrey A. Sabby[4,6], and Antonio Claret[5]
[1] Physics Department, University of Arkansas, Fayetteville, AR 72701, USA; clacy@uark.edu
[2] Harvard-Smithsonian Center for Astrophysics, 60 Garden Street, Cambridge, MA 02138, USA; gtorres@cfa.harvard.edu
[3] Center of Excellence in Information Systems, Tennessee State University, Nashville, TN 37209, USA; fekel@evans.tsuniv.edu
[4] Physics Department, Southern Illinois University Edwardsville, Edwardsville, IL 62026, USA; jsabby@siue.edu
[5] Instituto de Astrofisica de Andalucia, CSIC, Apdo. Postal 3004, E-18080 Granada, Spain; claret@iaa.es
Received 2012 February 9; accepted 2012 March 15; published 2012 April 30

ABSTRACT

BF Dra is now known to be an eccentric double-lined F6+F6 binary star with relatively deep (0.7 mag) partial eclipses. Previous studies of the system are improved with 7494 differential photometric observations from the URSA WebScope and 9700 from the NFO WebScope, 106 high-resolution spectroscopic observations from the Tennessee State University 2 m automatic spectroscopic telescope and the 1 m coudé-feed spectrometer at Kitt Peak National Observatory, and 31 accurate radial velocities from the CfA. Very accurate (better than 0.6%) masses and radii are determined from analysis of the two new light curves and four radial velocity curves. Theoretical models match the absolute properties of the stars at an age of about 2.72 Gyr and [Fe/H] = −0.17, and tidal theory correctly confirms that the orbit should still be eccentric. Our observations of BF Dra constrain the convective core overshooting parameter to be larger than about 0.13 H_p. We find, however, that standard tidal theory is unable to match the observed slow rotation rates of the components' surface layers.

Key words: binaries: eclipsing – binaries: spectroscopic – stars: fundamental parameters – stars: individual (BF Dra)

Online-only material: machine-readable and VO tables

1. INTRODUCTION

Eclipsing binary stars provide critical information that can be used to test our current theories of stellar evolution. By measuring accurately the changes in brightness over time (the light curve), times of minimum light (the ephemeris curve), and the pattern of changing radial velocities of the components (the radial velocity curve), orbital parameters may be determined including the masses, radii, luminosities, and internal structure constant. Additionally, the projected rotation rates ($v \sin i$) of the components may be measured from high-resolution spectra. These observationally determined values can then be compared with theoretical results from the current theory of stellar evolution to gauge the degree of completeness of the theory. These are the main goals of this type of investigation. A general compilation and investigation of the results from these types of studies are given by Torres et al. (2010).

The detached eccentric main-sequence eclipsing binary star BF Dra (BD +69 1006, GSC 04435−01750) is a relatively bright star ($V = 9.82$ mag), originally classified as F8 but now known to be F6+F6. It was first discovered as a variable star (BV379) by Strohmeier et al. (1962). Its orbital period was estimated by Doppner (1962) as 5.60571 days and refined by Strohmeier et al. (1963) to 5.60545 days. This period is wrong. The essentially correct period, about twice the first estimates, is given by Imbert (1985) from spectral analysis as 11.2109 days, improved by eclipse observations to 11.211079 days, by Diethelm et al. (1993). Our current study is based on the analysis of 76 dates of minimum light, a large number (137) of new high-resolution spectrograms, combined with a very large number (7494+9700) of new differential magnitudes obtained by two different robotic telescopes. These new results are more definitive that in previous studies, and are accurate to better than 0.6% in the masses and radii. The new spectroscopic study is discussed in Section 2, the photometric study in Section 3, and the absolute properties and comparison to theory in Section 4.

2. SPECTROSCOPIC STUDY

2.1. Spectroscopic Observations and Reductions

The spectroscopic observations at the Harvard-Smithsonian Center for Astrophysics (CfA) were carried out with two different spectrographs on the 1.5 m Tillinghast reflector at the F. L. Whipple Observatory on Mount Hopkins, AZ. Eighteen spectra were gathered by Torres between 2006 April and 2009 May with a Cassegrain-mounted echelle spectrograph ("Digital Speedometer" (DS); Latham 1992) equipped with a photon-counting Reticon detector that recorded a single echelle order 45 Å wide centered at a wavelength near 5187 Å (Mg I b triplet), with a resolving power of $R \sim 35{,}000$. The signal-to-noise ratios of these spectra range from 23 to 33 per resolution element of 8.5 km s^{-1}. Thirteen additional spectra covering the interval 3860–9100 Å were collected between 2010 March and 2011 November with the bench-mounted fiber-fed echelle instrument TRES (Furesz 2008), at a resolving power of $R \sim 48{,}000$ and with signal-to-noise ratios of ranging from 19 to 92 per resolution element of 6.2 km s^{-1}. The average exposure time for both the TRES and DS spectra was 15 minutes.

Radial velocities were derived from these observations by using the two-dimensional cross-correlation technique TODCOR (Zucker & Mazeh 1994), in the same manner as described recently by Torres et al. (2012). The measurements of Torres are given in Table 1. The light ratio inferred from these spectra is $L_B/L_A = 0.88 \pm 0.02$ at the mean wavelength of 5187 Å, near

[6] Visiting Astronomer, Kitt Peak National Observatory, National Optical Astronomy Observatories, operated by the Association of Universities for Research in Astronomy, Inc. under a cooperative agreement with the National Science Foundation.
[7] The research at Tennessee State University was supported in part by NASA, NSF, Tennessee State University, and the state of Tennessee through its Centers of Excellence program.

Table 1
Radial Velocities of BF Dra and Residuals from the Fitted Orbit

HJD−2,400,000	Orbital Phase	RV_A (km s^{-1})	RV_B (km s^{-1})	$O-C_1$ (km s^{-1})	$O-C_2$ (km s^{-1})	Observatory/Instrument
Observations from the TSU						
55298.890	0.5909	−51.7	−7.3	−0.41	0.61	Fairborn
55300.751	0.7569	−86.0	27.6	−0.16	−0.02	Fairborn
55327.650	0.1562	42.0	−102.9	0.43	0.49	Fairborn
55338.811	0.1517	41.7	−104.9	−0.35	−1.02	Fairborn
55355.902	0.6762	−69.8	11.5	−0.39	0.78	Fairborn
55366.924	0.6594	−66.2	7.3	−0.35	0.24	KPNO
55367.896	0.7461	−84.2	25.1	−0.45	−0.36	KPNO
55368.856	0.8317	−97.7	39.6	0.00	−0.21	KPNO
55369.862	0.9214	−90.9	31.9	−0.27	−0.64	KPNO
55370.949	0.0184	−8.3	−52.3	−0.17	−0.01	KPNO
55463.654	0.2875	15.4	−76.2	−0.09	0.38	KPNO
55464.724	0.3829	−5.7	−54.4	0.49	−0.12	KPNO
55569.645	0.7417	−84.0	24.3	−1.11	−0.28	Fairborn
55573.013	0.0421	13.5	−75.6	−0.66	−0.39	Fairborn
55575.925	0.3019	11.6	−73.1	−0.61	0.10	Fairborn
55578.957	0.5723	−47.7	−11.7	−0.36	0.27	Fairborn
55581.930	0.8375	−98.6	40.9	−0.33	0.50	Fairborn
55582.902	0.9242	−90.7	31.1	−1.16	−0.31	Fairborn
55584.970	0.1087	42.7	−104.7	0.15	−0.30	Fairborn
55587.890	0.3691	−2.8	−57.4	0.29	0.07	Fairborn
55607.910	0.1549	42.7	−103.8	0.98	−0.25	Fairborn
55640.916	0.0989	40.7	−102.9	−0.48	0.09	Fairborn
55643.814	0.3574	1.0	−59.8	1.46	0.38	Fairborn
55646.796	0.6234	−57.7	−0.1	0.53	0.67	Fairborn
55647.842	0.7167	−78.4	18.9	−0.55	−0.50	Fairborn
55648.815	0.8035	−95.2	36.3	−1.19	0.28	Fairborn
55655.795	0.4261	−15.2	−44.4	0.58	0.03	Fairborn
55657.868	0.6110	−55.6	−3.3	0.00	0.18	Fairborn
55659.775	0.7811	−90.4	32.9	−0.08	0.68	Fairborn
55662.750	0.0465	17.5	−78.8	−0.11	−0.05	Fairborn
55666.771	0.4052	−9.9	−49.7	1.25	−0.51	Fairborn
55669.636	0.6607	−65.9	6.9	0.24	−0.46	Fairborn
55670.971	0.7798	−91.3	32.4	−1.22	0.43	Fairborn
55679.969	0.5824	−49.2	−10.2	0.29	−0.44	KPNO
55681.706	0.7373	−82.1	23.2	−0.08	−0.49	Fairborn
55682.698	0.8258	−97.2	40.1	−0.15	0.96	Fairborn
55683.730	0.9179	−93.0	33.3	−1.09	−0.55	Fairborn
55684.944	0.0262	0.4	−60.3	0.63	0.11	Fairborn
55691.901	0.6467	−62.9	3.8	0.28	−0.51	Fairborn
55697.791	0.1721	39.9	−102.4	0.46	−1.20	Fairborn
55699.945	0.3642	−1.3	−58.4	0.69	0.20	Fairborn
55708.713	0.1463	42.5	−104.1	−0.06	0.31	Fairborn
55709.698	0.2342	27.4	−89.2	−0.09	−0.29	Fairborn
55710.681	0.3218	7.4	−68.2	−0.23	0.29	Fairborn
55711.682	0.4111	−11.7	−47.1	0.77	0.72	Fairborn
55717.684	0.9465	−77.2	18.9	0.54	−0.39	Fairborn
55719.684	0.1249	44.0	−104.9	0.56	0.42	Fairborn
55721.713	0.3059	10.9	−71.5	−0.38	0.75	Fairborn
55726.853	0.7644	−87.9	29.1	−0.63	0.02	Fairborn
55728.818	0.9396	−81.9	23.5	0.07	−0.14	Fairborn
55735.742	0.5572	−44.1	−14.8	0.03	0.48	Fairborn
55743.941	0.2886	15.2	−75.7	−0.04	0.62	Fairborn
Observations from the UofA						
47653.9211	0.6742	−69.2	10.2	−0.27	0.25	KPNO coudé feed
47655.9119	0.8517	−100.2	41.4	−0.64	−0.04	KPNO coudé feed
47656.8072	0.9316	−85.5	29.0	1.29	0.68	KPNO coudé feed
48014.7902	0.8630	−99.4	42.1	0.55	0.26	KPNO coudé feed
48016.7805	0.0405	13.3	−72.4	1.07	1.10	KPNO coudé feed
48017.8572	0.1366	43.6	−104.8	0.67	0.27	KPNO coudé feed
50940.8619	0.8630	−99.6	40.8	0.29	−0.98	KPNO coudé feed
50943.7953	0.1247	42.1	−107.3	−1.10	−1.96	KPNO coudé feed
50944.7869	0.2131	29.1	−93.8	−2.74	−0.13	KPNO coudé feed
51243.9567	0.8985	−97.3	38.8	−0.06	−0.26	KPNO coudé feed

Table 1
(Continued)

HJD−2,400,000	Orbital Phase	RV_A (km s^{-1})	RV_B (km s^{-1})	$O-C_1$ (km s^{-1})	$O-C_2$ (km s^{-1})	Observatory/Instrument
51246.9510	0.1656	40.1	−101.7	−0.12	0.58	KPNO coudé feed
51246.9938	0.1694	39.4	−101.0	−0.28	0.73	KPNO coudé feed
51247.0325	0.1729	38.6	−101.0	−0.57	0.20	KPNO coudé feed
51248.0319	0.2620	20.2	−82.9	−1.04	−0.14	KPNO coudé feed
51248.9460	0.3436	2.5	−63.7	−0.17	−0.03	KPNO coudé feed
51309.9451	0.7846	−91.6	32.9	−0.57	0.23	KPNO coudé feed
51310.8545	0.8657	−100.2	41.7	−0.30	−0.10	KPNO coudé feed
51311.7901	0.9491	−76.2	17.0	0.18	−0.62	KPNO coudé feed
51313.7776	0.1264	43.6	−105.3	0.38	0.06	KPNO coudé feed
51314.7948	0.2171	30.5	−93.1	−0.52	−0.28	KPNO coudé feed
51314.8820	0.2249	29.4	−91.3	0.01	−0.16	KPNO coudé feed
51315.7526	0.3026	12.0	−74.2	−0.01	−0.93	KPNO coudé feed
51315.7947	0.3063	10.6	−72.8	−0.55	−0.41	KPNO coudé feed
51449.7263	0.2528	22.9	−84.8	−0.41	0.09	KPNO coudé feed
51449.7730	0.2569	21.5	−83.3	−0.87	0.63	KPNO coudé feed
51453.6741	0.6049	−54.6	−5.5	−0.30	−0.41	KPNO coudé feed
51453.7172	0.6088	−54.4	−4.9	0.72	−0.66	KPNO coudé feed
51453.7600	0.6126	−55.8	−3.4	0.14	0.01	KPNO coudé feed
51454.6624	0.6931	−72.7	14.5	0.30	0.37	KPNO coudé feed
51454.7129	0.6976	−73.7	14.7	0.24	−0.40	KPNO coudé feed
51455.6630	0.7823	−90.2	31.8	0.44	−0.47	KPNO coudé feed
51455.7119	0.7867	−90.7	33.5	0.70	0.45	KPNO coudé feed
51706.6868	0.1732	39.4	−100.9	0.27	0.25	KPNO coudé feed
51708.6891	0.3518	0.6	−61.5	−0.20	0.25	KPNO coudé feed
51708.7904	0.3608	−1.4	−58.9	−0.16	0.75	KPNO coudé feed
51789.7199	0.5796	−47.9	−11.0	1.00	−0.36	KPNO coudé feed
51790.7540	0.6718	−68.4	9.8	0.13	0.26	KPNO coudé feed
51791.7984	0.7650	−86.8	30.2	0.68	1.18	KPNO coudé feed
51792.7624	0.8509	−99.3	41.9	0.15	0.56	KPNO coudé feed
55478.6720	0.6271	−58.7	−0.3	0.44	−0.19	KPNO coudé feed
55478.6868	0.6284	−58.2	0.7	1.22	0.52	KPNO coudé feed
55478.7016	0.6297	−59.2	0.8	0.50	0.34	KPNO coudé feed
55479.6567	0.7149	−76.9	19.5	0.71	0.62	KPNO coudé feed
55479.6730	0.7164	−77.4	20.4	0.51	1.22	KPNO coudé feed
55479.6886	0.7178	−77.6	20.4	0.59	0.92	KPNO coudé feed
55480.5848	0.7977	−93.5	34.5	−0.26	−0.45	KPNO coudé feed
55480.6007	0.7991	−93.1	34.7	0.36	−0.48	KPNO coudé feed
55480.6162	0.8005	−93.8	34.7	−0.12	−0.70	KPNO coudé feed
55646.9021	0.6329	−60.5	0.7	−0.12	−0.46	KPNO coudé feed
55646.9236	0.6348	−60.9	0.8	−0.11	−0.78	KPNO coudé feed
55646.9472	0.6369	−60.7	1.7	0.53	−0.34	KPNO coudé feed
55646.9688	0.6388	−61.8	1.5	−0.16	−0.96	KPNO coudé feed
55646.9929	0.6410	−62.9	2.6	−0.80	−0.33	KPNO coudé feed
55647.0144	0.6429	−62.6	2.3	−0.09	−1.05	KPNO coudé feed
			Observations from the CfA			
53837.9981	0.2821	16.05	−78.34	−0.27	−0.23	DS
53842.9185	0.7210	−77.59	20.43	−0.64	0.39	DS
53870.9714	0.2232	29.73	−91.13	1.29	0.44	DS
53871.9180	0.3077	11.09	−71.76	0.55	0.34	DS
53899.8054	0.7952	−93.18	34.02	1.07	−0.42	DS
53922.8254	0.8485	−99.57	41.67	0.67	0.60	DS
53932.7896	0.7373	−82.55	23.13	0.29	−0.30	DS
53989.7064	0.8142	−96.52	36.14	−1.10	−1.25	DS
54021.6130	0.6602	−65.35	7.45	−2.74	0.47	DS
54071.5559	0.1150	43.88	−105.47	−0.06	−0.33	DS
54247.8956	0.8442	−99.19	41.06	−0.12	0.30	DS
54279.8524	0.6947	−72.93	14.67	−0.28	0.22	DS
54307.7595	0.1839	37.50	−101.10	−0.57	−1.66	DS
54577.9810	0.2872	15.82	−77.63	−1.04	−0.72	DS
54604.9131	0.6894	−71.68	13.75	−0.17	0.41	DS
54632.8458	0.1810	38.06	−99.62	−0.57	0.34	DS
54718.6172	0.8316	−98.69	40.16	−0.30	0.57	DS
54958.9020	0.2646	20.51	−83.32	0.18	−1.14	DS
55283.0156	0.1749	37.64	−101.10	0.38	−0.13	TRES

Table 1
(Continued)

HJD−2,400,000	Orbital Phase	RV_A (km s^{-1})	RV_B (km s^{-1})	$O-C_1$ (km s^{-1})	$O-C_2$ (km s^{-1})	Observatory/Instrument
55339.9664	0.2548	21.92	−83.48	−0.52	0.96	TRES
55345.9660	0.7900	−91.44	32.00	0.01	−1.55	TRES
55383.6645	0.1526	40.51	−103.84	−0.01	0.18	TRES
55401.8028	0.7705	−87.78	28.03	−0.55	−2.00	TRES
55402.6881	0.8495	−99.07	40.99	−0.41	−0.12	TRES
55463.5985	0.2826	17.26	−79.18	−0.87	−1.21	TRES
55496.5791	0.2244	28.22	−89.83	−0.30	1.47	TRES
55497.5812	0.3137	10.47	−72.26	0.72	−1.63	TRES
55692.7810	0.7252	−79.39	22.59	0.14	1.64	TRES
55698.9527	0.2757	18.01	−80.14	0.30	−0.57	TRES
55826.6182	0.6632	−68.30	9.50	0.24	1.81	TRES
55872.6149	0.7660	−86.57	27.46	0.44	−1.72	TRES
		Observations of Imbert (1985)				
43363.3875	0.9667	−58.9		4.11		CORAVEL
43364.4319	0.0599	26.7		0.81		CORAVEL
43366.4354	0.2386	28.9		2.28		CORAVEL
43367.3847	0.3233	6.6		−0.96		CORAVEL
43670.5342	0.3636	−1.8		−0.22		CORAVEL
43673.5737	0.6347	−62.2		−1.82		CORAVEL
43751.3853	0.5754	−48.6		−0.90		CORAVEL
43752.3857	0.6646	−66.0		0.75		CORAVEL
43753.3955	0.7547	−84.0		1.36		CORAVEL
43754.3604	0.8408	−98.7		0.07		CORAVEL
43755.3564	0.9296	−84.8		3.07		CORAVEL
43758.3643	0.1979	33.4		−1.54		CORAVEL
43759.3521	0.2860	18.8		2.78		CORAVEL
44297.6689	0.3028	11.4		−0.78		CORAVEL
44298.6361	0.3891	−5.9		1.40		CORAVEL
44332.5908	0.4178	−11.3		2.36		CORAVEL
44334.5908	0.5962	−52.1		0.07		CORAVEL
4470.3516	0.7058	−78.6		−3.15		CORAVEL
44471.3525	0.7951	−94.2		−1.47		CORAVEL
44472.3330	0.8826	−101.0		−1.58		CORAVEL
44475.3252	0.1495	42.3		0.23		CORAVEL
44683.6182	0.7288	−80.8		−0.60		CORAVEL
44854.3037	0.9536	−74.4		−0.85		CORAVEL
44855.3096	0.0433	11.8		−2.58		CORAVEL
44909.3486	0.8635	−99.1		0.85		CORAVEL
44910.2598	0.9448	−81.3		−1.73		CORAVEL
44911.2832	0.0361	8.6		0.36		CORAVEL
45012.7012	0.0824	34.9		−1.53		CORAVEL
45015.6348	0.3440	2.3		−0.50		CORAVEL
45063.4980	0.6133	−57.6		−1.75		CORAVEL
45066.6338	0.8931	−101.3		−3.03		CORAVEL
45067.4854	0.9690	−58.7		2.14		CORAVEL
45068.4619	0.0561	24.8		1.15		CORAVEL
45136.3662	0.1131	41.7		−0.89		CORAVEL
		Observations of Imbert (1985)				
43363.4145	0.9691		0.3		−1.47	CORAVEL
43364.4465	0.0612		−90.2		−1.99	CORAVEL
43366.4243	0.2376		−88.3		0.09	CORAVEL
43367.3965	0.3243		−66.8		1.53	CORAVEL
43673.5703	0.6344		0.7		−0.52	CORAVEL
43751.3979	0.5765		−12.6		−1.09	CORAVEL
43752.3936	0.6653		6.6		−1.39	CORAVEL
43753.4038	0.7554		28.0		0.88	CORAVEL
43754.3545	0.8402		43.1		2.40	CORAVEL
43755.3628	0.9302		30.0		0.72	CORAVEL
43758.3721	0.1986		−94.2		2.40	CORAVEL
43759.3457	0.2854		−77.9		−0.50	CORAVEL
44297.6641	0.3024		−71.8		1.62	CORAVEL
44298.6285	0.3884		−53.6		−0.15	CORAVEL
44332.5754	0.4164		−50.1		−3.03	CORAVEL

Table 1
(Continued)

HJD−2,400,000	Orbital Phase	RV_A (km s^{-1})	RV_B (km s^{-1})	$O-C_1$ (km s^{-1})	$O-C_2$ (km s^{-1})	Observatory/Instrument
44334.5859	0.5958		−5.0		2.26	CORAVEL
44470.3438	0.7051		15.6		−1.03	CORAVEL
44471.3467	0.7946		32.0		−2.46	CORAVEL
44472.3291	0.8822		40.1		−1.35	CORAVEL
44475.3193	0.1489		−99.4		4.71	CORAVEL
44683.6133	0.7284		20.3		−1.27	CORAVEL
44854.3135	0.9545		10.6		−3.55	CORAVEL
44855.3154	0.0439		−78.3		−2.29	CORAVEL
44909.3428	0.8630		43.3		1.34	CORAVEL
44910.2549	0.9444		23.9		2.61	CORAVEL
44911.2773	0.0355		−67.2		1.59	CORAVEL
45012.6934	0.0817		−98.7		−0.68	CORAVEL
45015.6250	0.3432		−63.7		0.18	CORAVEL
45063.4844	0.6121		−3.8		−0.16	CORAVEL
45066.6250	0.8923		43.1		2.75	CORAVEL
45067.4785	0.9684		2.9		0.58	CORAVEL
45068.4531	0.0553		−85.4		−0.81	CORAVEL
45136.3604	0.1125		−104.3		0.25	CORAVEL

Note. Star A, the spectroscopic primary star, is the more massive, larger, and cooler one.

the visual band. This value is close to the one determined by analysis of the light curves (0.873 ± 0.009 in the *V* band, see Section 3.4).

At Fairborn Observatory from 2010 April through 2011 June, Fekel acquired 44 double-lined spectra with the Tennessee State University (TSU) 2 m automatic spectroscopic telescope (AST), a fiber fed echelle spectrograph, and a 2048 × 4096 SITe ST-002A CCD (Eaton & Williamson 2007). The echelle spectrograms have 21 orders that cover the wavelength range 4920–7100 Å. The resolution depended on the fiber used, and was either 0.24 or 0.4 Å, which produced typical signal-to-noise ratios of 25 and 35, respectively, at 6000 Å. Typical exposure times were 60 minutes for both Kitt Peak National Observatory (KPNO) and Fairborn spectra of BF Dra. From 24 of the best spectrograms, the equivalent-width ratio of the hotter to the cooler spectral component was 0.842 ± 0.009, which should be close to the light ratio in the *V* band, which it is (see Section 3.4).

In addition, between 2010 June and 2011 April, Fekel of TSU obtained eight additional double-lined spectra with the KPNO coudé feed telescope, coudé spectrograph, and a CCD. The first seven were acquired with a TI CCD consisting of an 800 × 800 array of 15 μm pixels. The spectra are centered at 6430 Å, cover a wavelength range of 84 Å, and have a resolution of 0.21 Å. The final spectrum was obtained with a CCD made by Semiconductor Technology Associates and designated STA2. It consists of a 2600 × 4000 array of 12 μm pixels. With STA2 the spectrum was once again centered at 6430 Å, and the much larger size of the detector produced a wavelength range of 336 Å. The spectrograph slit was set so that the STA2 spectrum has the same resolution as those acquired with the TI CCD although there is some worsening of the resolution at both ends of the spectrum. All the KPNO spectra have signal-to-noise ratios of about 100.

Fekel et al. (2009) have provided an extensive general description of the velocity measurement for the Fairborn Observatory echelle spectra. We used a line list for solar-type stars, and the resulting velocities are on an absolute scale. Our unpublished measurements of several IAU solar-type velocity standards indicate that the Fairborn Observatory velocities have a small zero-point offset of −0.3 km s^{-1} relative to the velocities of Scarfe (2010). Thus, we have added 0.3 km s^{-1} to each Fairborn velocity.

Tomkin & Fekel (2006) have discussed the measurement of the KPNO coudé spectra. The KPNO velocities are relative velocities that have been determined by cross-correlation with the IAU radial velocity standard stars HR 5694 and HR 7560. From Scarfe (2010) we adopt velocities of 54.4 and 0.0 km s^{-1}, respectively, for the standards. The Fairborn and KPNO observations and velocities of Fekel are listed in Table 1.

Lacy and Sabby of the University of Arkansas (UofA) obtained additional spectra at the KPNO coudé-feed spectrometer with a variety of detectors (TI, Ford, STA) from 1989 May to 2011 March. The resolution was typically 0.3 Å in the 6430 Å region. The exposure times were typically 30–60 minutes. The S/N was about 50. A typical spectrogram is shown in Figure 1.

Radial velocities were obtained by cross-correlation techniques based on spectra the standard star β Vir, which has an adopted radial velocity of +4.4 km s^{-1} (Scarfe 2010). Only unblended regions of the binary star spectrum were included in the cross-correlation analysis. The 54 resulting pairs of radial velocities are given in Table 1. The equivalent width ratio of the hotter to the cooler component's spectral lines was measured on each spectrogram for four different line pairs. The mean and standard error of the mean was 0.84 ± 0.02 at 6430 Å in the red, fairly consistent (1.5σ difference) with the light ratio derived from *V*-band photometry in Section 3.4.

All of the spectroscopic light-ratio estimates were made at somewhat different wavelengths, but since the temperature difference turns out to be very small (only 36 K) one does not expect a big difference in light ratio anyway, and this justifies just taking an average. The mean spectroscopic value and uncertainty are 0.854 ± 0.013, which may be compared with the adopted light curve results of 0.873 ± 0.009, which carries about twice the statistical weight of the spectroscopic result. The two different estimates do overlap within their joint uncertainties.

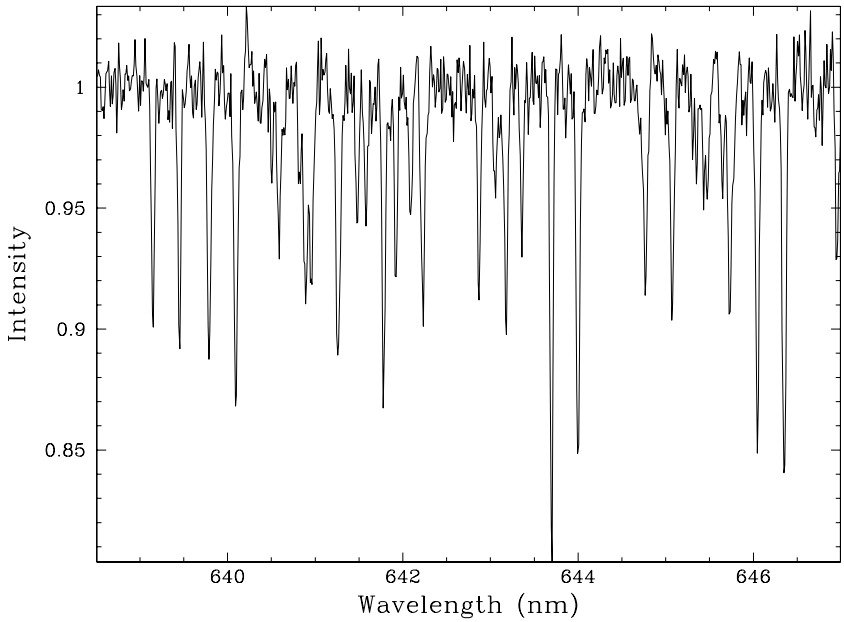

Figure 1. Typical KPNO coudé-feed spectrogram of BF Dra in a double-lined phase. In the line pairs, the rightmost component is due to the more massive, more luminous, larger, but cooler component of the binary.

2.2. Spectroscopic Orbit

The new radial velocities as measured at the TSU (KPNO+Fairborn), UofA (KPNO coudé feed), and CfA (DS+TRES) are supplemented by the radial velocities of Imbert (1985, CORAVEL). These four sets of velocities in Table 1 were analyzed to fit a spectroscopic orbit by using a least-squares technique that allowed for the fact that the different sets of velocities might have different zero points, and the velocities of the primaries in each set might have a different standard error than the secondaries in that set. It was also possible that the radial velocity zero point of the primaries within a set would be different from those of the secondaries within the same set, but when this proved not to be the case for any of the sets, it was fixed at zero for the final fit. In the end, the radial-velocity zero points were consistent to within 0.14 km s^{-1}, which is quite remarkable. In fitting the orbit, the orbital period was fixed at the value determined in Section 3, 11.2110011 days. Also, an apsidal motion of 1.°60 century^{-1} was assumed based on the ephemeris-curve solution below. Parameters that were varied include the center-of-mass velocity (γ), in the TSU reference frame; the radial-velocity semi-amplitudes (K_1 and K_2); the orbital eccentricity (e); and the longitude of periastron (ω) at the reference epoch T. The time of the deeper eclipse was fixed at the photometric value of HJD 2,454,204.79867. The method of Levenberg–Marquardt was used in the fitting throughout this paper, and the parameter error estimates were computed by the method. In estimating the errors of the fitted parameters, it is important that the reduced chi-square value of the residuals is unity, and this was imposed by scaling the assumed errors appropriately when necessary. The fitted parameters and uncertainties, as well as auxiliary quantities, are listed in Table 2 and shown in Figure 2.

Table 2
Spectroscopic Orbital Elements and Related Parameters of BF Dra

Parameter	Value	
	Star A	Star B
P[a] (days)	11.2110011 (adopted)	
T_0[b] (HJD Min I)	2, 454,204.79867 (adopted)	
T (HJD periastron)	2,455,460.47658 ± 0.00022	
e	0.3865 ± 0.0007	
ω_A (deg)	273.64 ± 0.10	
K (km s^{-1})	71.56 ± 0.08	73.58 ± 0.08
γ (km s^{-1})	−29.90 ± 0.05	
$m \sin^3 i$ (solar masses)	1.413 ± 0.004	1.374 ± 0.003
$a \sin i$ (Gm)	10.174 ± 0.011	10.462 ± 0.010
Zero-point offset (km s^{-1}):		
TSU-UofA	+0.14 ± 0.08	
TSU-CfA[c]	+0.22 ± 0.12	
TSU-Imbert	+0.08 ± 0.23	
Standard error (km s^{-1}):		
TSU	0.60	0.48
UofA	0.67	0.63
CfA	0.78	1.02
Imbert	1.78	1.87
Number of primary and secondary observations:		
TSU	52	52
UofA	54	54
CfA	31	31
Imbert	34	33

Notes.
[a] Photometric period.
[b] Photometric date of the deeper minimum.
[c] This offset, corrected to the absolute frame of reference of minor planets, is only +0.08 ± 0.12 km s^{-1}.

2.3. Spectral Types and Rotational Velocities

We have adopted a mean spectral type of F6 (T = 6380 ± 150 K) based on the absolute *uvbyβ* photometry of Section 3 (T = 6250 ± 150 K from the calibration of Popper 1980), and the optimum temperature determined in finding the CfA radial velocities by the TODCOR method, 6500 ± 150 K. The uncertainty of the adopted value is large enough to include the two different estimates. The uncertainty estimate from the photometry is based directly on the observational uncertainties

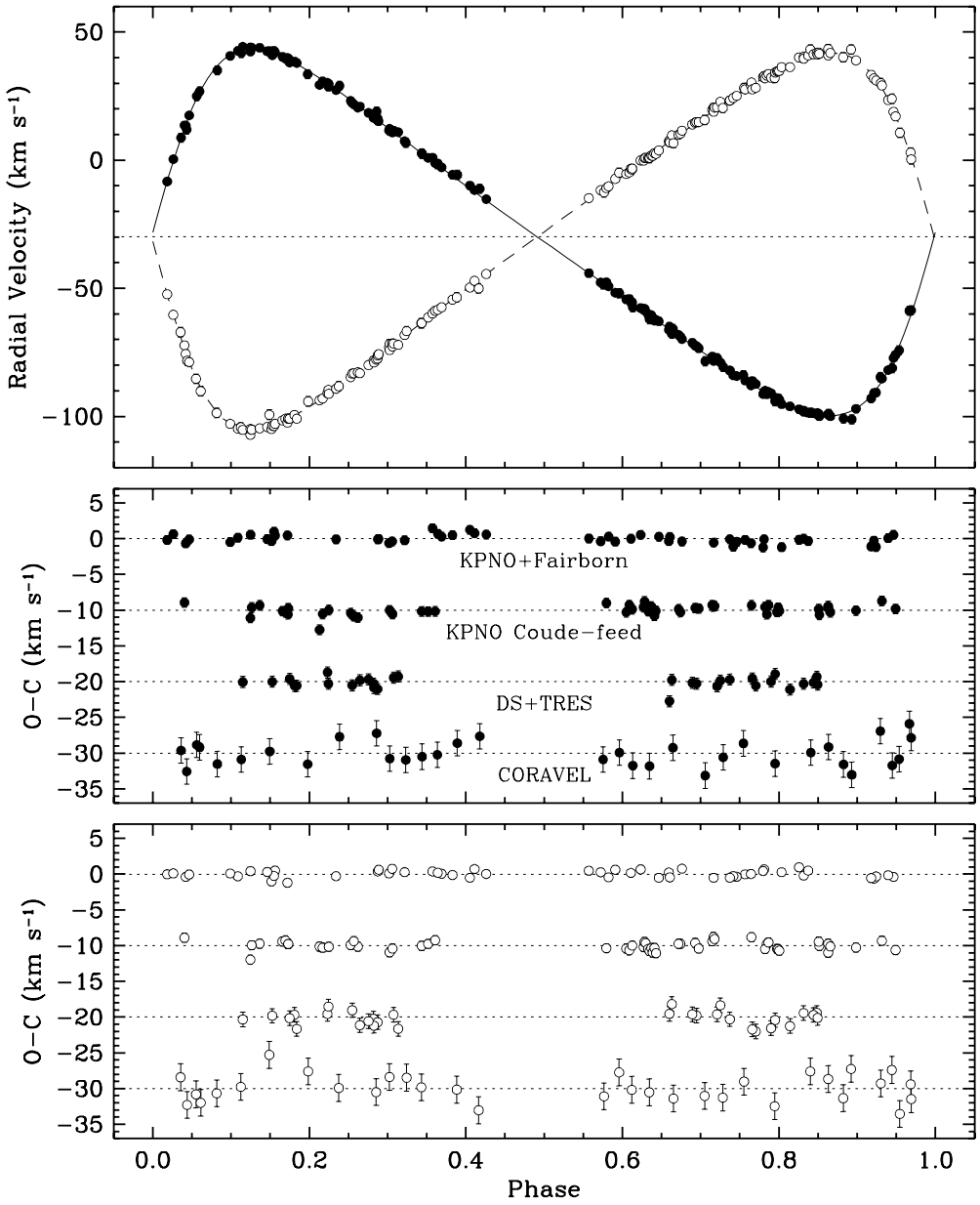

Figure 2. Radial velocities and the fitted orbits for BF Dra. Filled and open symbols represent the primary (more massive star) and secondary, respectively. Residuals are shown in the bottom two panels, with those from three of the data sets shifted vertically from an average of zero for clarity. Zero phase corresponds to the epoch of the deeper minimum (see Section 3.1).

in the photometric indices, plus an additional 50 K to allow for systematic error in the temperature calibration of Popper (1980, Table 1). The uncertainty in the TODCOR method is based on the variations with temperature, surface gravity, and chemical abundance of the cross-correlations between observed spectra and theoretical spectra.

Rotational velocity values were estimated by matching the profiles of the binary components' spectral lines with synthetically broadened lines of a narrow-lined standard star of the same spectral type, taken with the same spectroscopic settings. Following the procedure of Fekel (1997), we compute average $v \sin i$ values of 11.0 ± 1.0 and 9.5 ± 1.0 km s^{-1} for A and B, respectively, in Fekel's spectra, where the uncertainties are estimated from the range of estimates of different spectral lines. Lacy estimates corresponding $v \sin i$ values of 8.3 ± 1.0 and 7.3 ± 1.0 km s^{-1} for the components of BF Dra. He used β Vir and ι Psc as narrow-lined standards. He adopted values of $v \sin i = 5.4$ km s^{-1} (including microturbulence) for β Vir and 6.4 km s^{-1} for ι Psc. Torres estimates 12.2 ± 1.0 and 10.2 ± 1.0 km s^{-1} for the BF Dra components. We adopt the means and uncertainties, 10.5 ± 1.8 and 9.0 ± 1.8 km s^{-1}, where the rather poor agreement between our individual estimates is reflected in the larger adopted uncertainties.

3. PHOTOMETRIC STUDY

3.1. Times of Minimum Light and the Ephemeris Curve Solution

Published times of minimum light for BF Dra have been collected in Table 3 and analyzed by using the least-squares method of Lacy (1992). This method allows one to accurately estimate many of the orbital parameters of the binary star and their uncertainties by using an iterated least-squares fitting algorithm applied to the observed dates of minima, taking into

Table 3
Times of Eclipse of BF Dra and Residuals from the Ephemeris Curve Fit

Year	HJD −2,400,000	Precision (days)	Cycle Number	Eclipse Type[a]	$O-C$ (days)	Method	Ref.
1931.8	26631.317	0.03	−2573	2	0.09184	pg	1
1931.8	26631.340	0.03	−2573	2	0.11484	pg	1
1932.6	26928.423	0.03	−2546	1	−0.01656	pg	1
1933.6	27281.437	0.03	−2515	2	−0.02458	pg	1
1933.6	27298.437	0.03	−2513	1	0.03449	pg	1
1935.7	28066.378	0.03	−2445	2	0.14833	pg	1
1937.8	28834.315	0.03	−2376	1	0.00571	pg	1
1938.7	29159.324	0.03	−2347	1	−0.10425	pg	1
1946.2	31911.61	0.03	−2102	2	0.01667	pg	2
1953.3	34473.42	0.03	−1873	1	−0.02150	pg	2
1953.9	34714.46	0.03	−1852	2	0.12348	pg	2
1956.6	35695.40	0.03	−1764	1	−0.04033	pg	2
1957.4	35992.50	0.03	−1738	2	0.11259	pg	2
1958.3	36317.53	0.03	−1709	2	0.02438	pg	2
1958.3	36317.550	0.03	−1709	2	0.04438	pg	1
1958.3	36317.597	0.03	−1709	2	0.09138	pg	1
1958.6	36435.38	0.03	−1698	1	0.01377	pg	2
1959.6	36805.41	0.03	−1665	1	0.08082	pg	2
1960.6	37169.42	0.03	−1633	2	−0.11955	pg	2
1961.5	37483.428	0.03	−1605	2	−0.01879	pg	1
1961.7	37545.36	0.03	−1599	1	0.10493	pg	2
1961.7	37556.40	0.03	−1598	1	−0.06607	pg	2
1980.7	44490.321	0.005	−980	2	0.01623	vis	3
1988.3	47276.3948	0.0010	−731	1	−0.00691	pe	4
1989.5	47702.434	0.005	−693	1	0.01435	vis	5
1992.3	48722.615	0.002	−602	1	−0.00551	pe	6
1992.3	48722.616	0.002	−602	1	−0.00451	pe	6
1992.7	48868.3680	0.0004	−589	1	0.00451	pe	7
1995.9	50034.3094	0.0010	−485	1	0.00207	pe	8
1997.7	50712.3895	0.0010	−425	2	−0.00516	pe	9
2001.7	52147.40	0.02	−297	2	0.00082	pe	10
2002.4	52416.46183	0.0001	−273	2	−0.00070	pe	11
2002.7	52534.3595	0.0003	−262	1	−0.00048	pe	11
2002.9	52618.2608	0.0002	−255	2	0.00076	pe	11
2003.0	52657.6784	0.0004	−251	1	−0.00256	pe	11
2003.0	52657.6811	0.0005	−251	1	0.00014	pe	11
2003.4	52769.7901	0.0001	−241	1	−0.00084	pe	12
2003.5	52814.6354	0.0003	−237	1	0.00046	pe	12
2003.6	52859.4784	0.0004	−233	1	−0.00053	pe	11
2003.7	52898.5355	0.0004	−230	2	0.00114	pe	11
2004.9	53341.55151	0.00022	−190	1	−0.00036	pe	13
2004.9	53341.5523	0.0001	−190	1	0.00044	pe	14
2005.3	53464.87251	0.00012	−179	1	−0.00034	pe	13
2005.4	53503.9275	0.0004	−176	2	0.00061	pe	13
2005.7	53638.45808	0.0053	−164	2	−0.00048	pe	15
2005.7	53638.45877	0.0054	−164	2	0.00021	pe	15
2005.7	53638.45947	0.0052	−164	2	0.00091	pe	15
2005.7	53638.46016	0.0053	−164	2	0.00160	pe	15
2006.4	53868.46854	0.0001	−143	1	−0.00025	pe	11
2006.8	54019.6359	0.0006	−130	2	0.00426	pe	16
2006.8	54036.6322	0.0002	−128	1	−0.00157	pe	16
2007.4	54260.8543	0.0005	−108	1	0.00057	pe	17
2007.6	54305.6982	0.0003	−104	1	0.00047	pe	17
2007.7	54344.7510	0.0006	−101	2	0.00115	pe	17
2007.7	54361.7525	0.0004	−99	1	−0.00022	pe	17
2007.8	54389.5933	0.0012	−97	2	−0.00044	pe	18
2007.8	54406.5972	0.0003	−95	1	0.00049	pe	17
2007.8	54406.5976	0.0002	−95	1	0.00089	pe	17
2008.4	54613.8163	0.0004	−77	2	0.00311	pe	17
2008.5	54664.4498	0.0001	−72	1	0.00012	pe	11
2008.7	54731.7160	0.0002	−66	1	0.00033	pe	17
2008.9	54793.192	0.001	−61	2	0.00324	pe	11
2008.9	54804.3994	0.0008	−60	2	−0.00033	pe	11
2008.9	54810.1931	0.0007	−59	1	0.00044	pe	11
2009.3	54933.51406	0.0005	−48	1	0.00042	pe	11

Table 3
(Continued)

Year	HJD −2,400,000	Precision (days)	Cycle Number	Eclipse Type[a]	$O-C$ (days)	Method	Ref.
2009.3	54938.9325	0.0012	−48	2	0.00110	pe	17
2009.4	54978.3574	0.0008	−44	1	−0.00023	pe	11
2009.6	55034.4126	0.0001	−39	1	−0.00003	pe	19
2009.6	55034.4138	0.0004	−39	1	0.00117	pe	20
2009.7	55073.46141	0.0005	−36	2	−0.00167	pe	11
2010.5	55370.7426	0.0002	−9	1	0.00002	pe	21
2010.5	55370.7433	0.0003	−9	1	0.00072	pe	21
2010.8	55471.6415	0.0002	0	1	−0.00006	pe	21
2010.8	55471.6422	0.0002	0	1	0.00064	pe	21
2011.4	55695.8610	0.0002	20	1	−0.00053	pe	22
2011.6	55779.7569	0.0011	27	2	0.00254	pe	22

Notes.
[a] Eclipses of type 1 are the deeper eclipses when the hotter, less massive component (star B) is being eclipsed by the cooler, more massive component (star A).
References: (1) Strohmeier et al. 1963; (2) Doppner 1962; (3) Locher 1980; (4) Locher 1988; (5) Paschke 1989; (6) Hübscher 1992; (7) Diethelm 1993; (8) Diethelm 1996; (9) Agerer & Hübscher 1998; (10) Diethelm 2001; (11) Wolf et al. 2010; (12) Caton & Smith 2005; (13) Lacy 2006; (14) Smith & Caton 2007; (15) Brát et al. 2007; (16) Lacy 2007; (17) Lacy 2009; (18) Hübscher et al. 2008; (19) Hübscher et al. 2010a; (20) Hübscher et al. 2010b; (21) Lacy 2011; (22) this paper.

Table 4
Orbital Parameters Derived from or Assumed in Fits to the Dates of Minimum Light

Parameters	Fitted Values
e	0.3865 ± 0.0005
P_a (days)	11.2110047 ± 0.0000020
ω_A (deg)	273.62 ± 0.02
$\dot{\omega}$ (deg century^{-1})	1.60 ± 0.26
T_o (HJD − 2,400,000)[a]	55,471.64156 ± 0.00022
i (deg)	88.42 (fixed)
U (years)	22,400 ± 3,700

Note. [a] Time of the deeper minimum

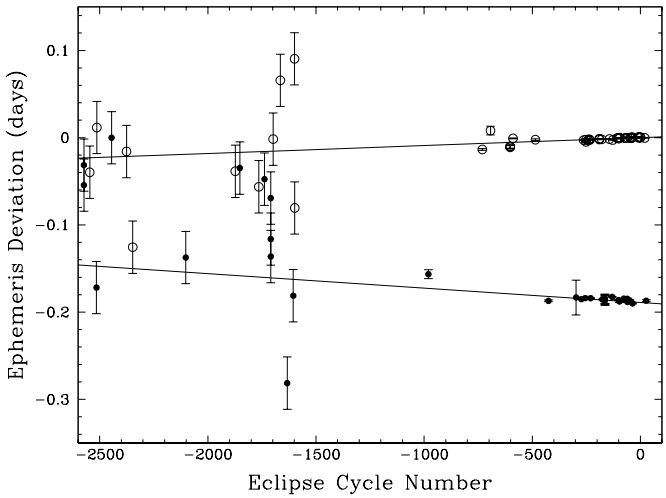

Figure 3. Ephemeris curve fit to all published dates of minimum light of BF Dra, covering an interval of about 80 years. Open circles are the deeper eclipses of the hotter star by the cooler star, and filled circles are the shallower eclipses of the cooler star by the hotter star. The early photographic minima on the left have poor accuracy relative to the recent CCD dates on the right. The apsidal motion period U is about 22,400 years.

account the published observational errors. The principal orbital parameters determined from fitting this so-called ephemeris curve are the eccentricity (e), anomalistic period (P_a), longitude of periastron (ω), apsidal motion rate ($\dot{\omega}$), reference time of minimum light (T_o). These five parameters are fitted to the data. The apsidal motion period (U) can be calculated easily from the apsidal motion rate. Apsidal motion in this binary system is due to both a classical Newtonian interaction and the general relativistic effect, both effects being about equally efficient.

Uncertainties in the dates of minima of a similar type (photographic, visual, photoelectric, or CCD) were adjusted (scaled) by the fitting method in order to result in a reduced chi-square of unity, which is a necessary step for the accurate estimation of the fitted orbital parameter uncertainties via the Levenberg–Marquardt method. The orbital parameters so determined are given in Table 4, and the fit is displayed in Figure 3. No noticeable pattern is evident in the residuals to the fit, which fact is consistent with the assumption that the binary system does not appear to have any additional close stellar components (a distant visual companion will be mentioned later, but it is too distant to affect the apsidal motion significantly).

Recent deeper minima (since HJD 2,452,534) observed with photoelectric or CCD equipment were fitted to a linear ephemeris by a least-squares method that also estimated the parameter errors by scaling the uncertainties to produce a reduced chi-square value of unity:

$$\text{HJD Min } I = 2{,}454{,}204.79867(10) + 11.2110011(12)E,$$

where the uncertainties in the last digits are given in parentheses. This linear ephemeris was adopted for the light curve analyses of recent photometry given below.

3.2. Interstellar Reddening and Mean Temperature

Color indices in the *uvbyβ* photometric system have been published by Lacy (2002) based on one set of measurements. This photometric system is designed to allow accurate estimation of the interstellar reddening. The β value places the mean spectral type in the F star region. The *uvbyβ* indices indicate that the primary and secondary are both F7 stars according to Popper's (1980) Table 1. Following the precepts of Crawford

Table 5
URSA Differential Photometry of BF Dra

Orbital Phase	ΔV	HJD − 2,400,000
0.34515	0.330	52314.00083
0.34523	0.326	52314.00175
0.34531	0.330	52314.00267
0.34539	0.334	52314.00359
0.34547	0.330	52314.00452

(This table is available in its entirety in machine-readable and Virtual Observatory (VO) forms in the online journal. A portion is shown here for guidance regarding its form and content.)

Table 6
NFO Differential Photometry of BF Dra

Orbital Phase	ΔV	HJD − 2,400,000
0.48261	0.790	53447.86110
0.48276	0.792	53447.86286
0.48292	0.790	53447.86457
0.48307	0.787	53447.86633
0.48323	0.785	53447.86808

(This table is available in its entirety in machine-readable and Virtual Observatory (VO) forms in the online journal. A portion is shown here for guidance regarding its form and content.)

& Barnes (1974) but using the standard relations of Perry & Johnson (1982), we find an interstellar reddening value of $E(b-y) = 0.019 \pm 0.010$ mag, where the reddening uncertainty is based on the observational errors in the color indices, and a visual absorption of $A_v = 0.082$ mag. The value of δm_1, through the calibration of Stromgren (1966), gives a surface value of the iron abundance [Fe/H] $= -0.03 \pm 0.15$, near solar abundance. The temperature calibration of Popper (1980), which is based primarily on that of Hayes (1978), gives a mean value of 6250 ± 150 K based on the value of $(b-y)_o$, whereas the calibration of Alonso et al. (1996) gives 6270 ± 100 K. The *difference* in the temperatures of the hotter and cooler components, $T_h - T_c$, is much more accurately known from the central surface brightness parameter *Jc* (see below) as 36 ± 10 K, following the method of Lacy (1987).

3.3. Differential Photometry

One of the telescopes used to obtain the differential photometry is the URSA WebScope, which consists of a Meade 10 inch $f/6.3$ LX-200 telescope with a Santa Barbara Instruments Group ST8 CCD camera (binned 2×2 to produce 765×510 pixel images with 2.3 arcsec square pixels) inside a Technical Innovations Robo-Dome, and controlled automatically by an Apple Macintosh G4 computer. The observatory is located on top of Kimpel Hall on the Fayetteville campus, with the control room directly beneath the observatory inside the building. 40–60 s exposures through a Bessel *V* filter (2.0 mm of GG 495 and 3.0 mm of BG 39) were read out and downloaded to the control computer over a 30 s interval, then the next exposure was begun. The observing cadence was therefore about 90 s per observation. The variable star would frequently be monitored continuously for 2–6 hr. BF Dra was observed by URSA on 115 nights during parts of 10 observing seasons from 2002 February 8 to 2011 September 26, yielding 7494 observations.

The other telescope we used is the NFO WebScope, a refurbished 24 inch Group 128 cassegrain reflector with a $2K \times 2K$ Kodak CCD camera, located near Silver City, NM (Grauer et al. 2008). Observations consisted of 60 s exposures through a Bessel *V* filter. BF Dra was observed by NFO on 248 nights during parts of seven observing seasons from 2005 March 18 to 2011 September 26, yielding 9700 observations.

The images were analyzed by a virtual measuring engine application written by Lacy that flat-fielded the URSA images (the NFO images are flat-fielded before distribution), automatically located the variable, comparison, and check stars in the image, measured their brightnesses, subtracted the corresponding sky brightness, and corrected for the differences in airmass between the stars. Extinction coefficients were determined nightly from the comparison star measurements. They averaged 0.25 mag airmass^{-1} at URSA (they ranged from 0.20 to 0.30 mag airmass^{-1}), 0.18 mag airmass^{-1} at the NFO (they ranged from 0.12 to 0.25 mag airmass^{-1}). The comparison stars were TYC 4435-0160-1 (BD +69° 1005, $V = 9.85$, F5) and TYC 4435-0426-1 ($V = 10.43$, K2:). Both comparison stars are within 8 arcmin of the variable star. The mean nightly comparison star magnitude differences were constant at the level of 0.008 mag (URSA) and 0.015 mag (NFO) for the standard deviation of the mean magnitude differences during a night, and 0.009 mag (URSA) and 0.007 mag (NFO) for the standard deviation of the nightly differential magnitudes. For the differential magnitudes, the sum of the fluxes of both comparison stars was converted to a magnitude called "comparisons." The resulting 7494 (URSA) and 9700 (NFO) *V* magnitude differences (variable-comparisons) are listed in Tables 5 and 6 (without any nightly corrections) and are shown in Figures 4–6 (after the nightly corrections discussed below have been added).

We noticed early on during the observations that the NFO magnitudes showed a small but significant offset from night to night, on the order of a hundredth of a magnitude. The origin of the offset is a variation in responsivity across the field of view of the NFO combined with imprecise centering from night to night. These variations are a well-known effect of the optics when using wide-field imaging telescopes such as the NFO. We have removed most of this variation by using dithered exposures of open star clusters to measure this variation, fitting a two-dimensional polynomial (see Selman 2004) and removing the variation during initial reductions (photometric flat). The URSA observations, moreover, show this kind of effect to a very much smaller extent than the NFO observations.

3.4. Photometric Orbit

The light curve fitting was done with the NDE model as implemented in the code *jktebop* (Etzel 1981; Popper & Etzel 1981; Southworth et al. 2007), and the linear ephemeris adopted is that of Section 3.1. The main adjustable parameters are the relative central surface brightness of the cooler star (J_A) in units of the central surface brightness of the hotter star, the sum of the relative radii of the cooler and hotter stars ($r_A + r_B$) in units of the separation, the ratio of radii ($k = r_A/r_B$), the inclination of the orbit (i), and the geometric factors $e \cos \omega$ and $e \sin \omega$ which account for the orbital eccentricity. Auxiliary parameters needed in the analysis include the gravity-brightening exponent, which we adopt as 0.32 for both the hotter and the cooler stars based on their temperatures (Claret 1998). For the analysis of the URSA data, quadratic limb-darkening coefficients (u, u') were adopted as the average of four recent theoretical values (Diaz-Cordoves et al. 1995; Claret 2000; Claret & Hauschildt 2003) because a quadratic limb-darkening law produced a better fit to

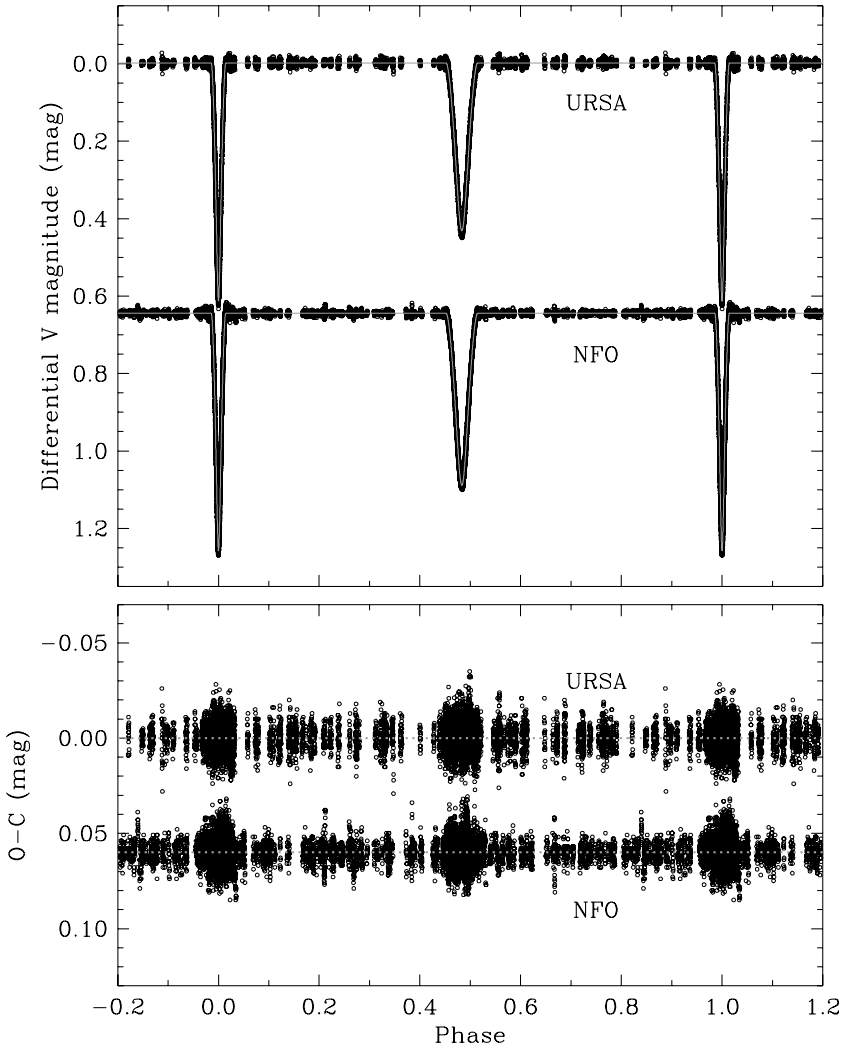

Figure 4. URSA and NFO light curves in *V* and residuals from the fitted models.

the data. For the analysis of the NFO data, no improvement was shown by using a nonlinear limb-darkening law, so an optimal linear law coefficient was fitted to the data by the jktebop algorithm. The mass ratio ($q = M_A/M_B = 1.028$) was adopted from the spectroscopic analysis in Section 2. Other adjusted parameters were the magnitude at quadrature and the phase of the deeper eclipse. The amount of "reflected light" was calculated from bolometric theory (see Popper & Etzel 1981). The fitting procedure converged to a solution for both the URSA and NFO data sets (Table 7).

Examination of the residuals showed that small but significant night-to-night residual variations remained in the NFO data even after application of the photometric flat, and to a much smaller extent, were also present in the URSA data. The fact that they are essentially absent from the URSA data, which were obtained contemporaneously with the NFO data, shows that they are not intrinsic variations in the stars' brightnesses, but are only optical effects due to the type of telescope used. We have applied nightly corrections, based on the initial photometric orbits, to the data sets to remove these observational effects. The number of nights on which these adjustments were made is listed in Table 7 as "Corrections." Fits to the "corrected" data then show significantly reduced residual variance, and we have adopted these improved fits (Table 7) for further use.

Although we used the average of four sets of quadratic limb-darkening values for the URSA fit because we thought they would be the best representatives of this limb-darkening formulation, the particular values of Claret (2000), Atlas models, do give a slight improvement in the residual variance of the light curve fit. The optimum fitted values of the radii in this case were changed by +0.4% for r_A and −0.9% for r_B. We consider the effect of this sensitivity to the limb-darkening values on our adopted error estimates below.

As a check on the accuracy of the parameter uncertainties estimated by the fitting method, we have done extensive Monte Carlo simulations in which pseudo-random observational errors of the appropriate standard deviation are added to the fitted model and the model parameters are then refit. This process is repeated 500 times (which takes about 6 hr of computing on our machine) and the statistics of the 500 fitted parameter sets are compiled to determine the parameter uncertainties to about two digits of accuracy. Most values of parameter uncertainty agreed between the original fitting method and the Monte Carlo method, but a few of them (for r_A, r_B, and e) did change somewhat. The adopted uncertainties in Table 7 take into account both the error estimates from the Monte Carlo method and the degree of agreement between the independent parameter values from the URSA and NFO telescopes.

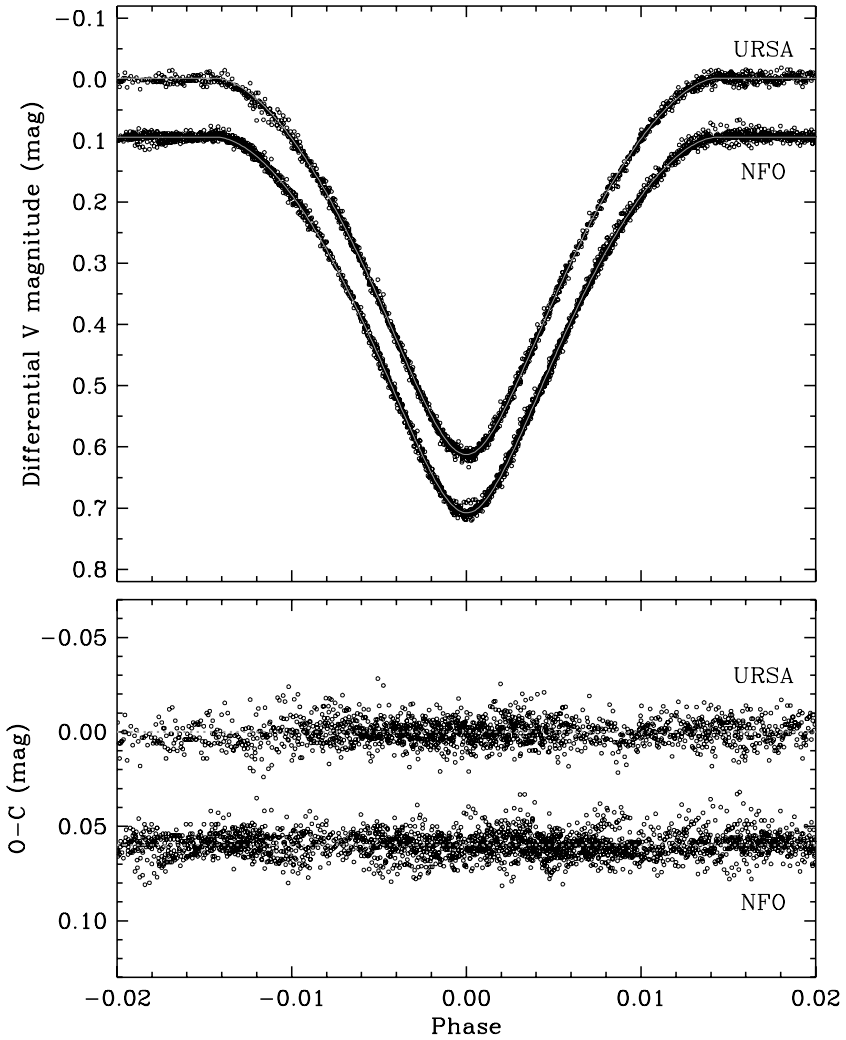

Figure 5. Close-up of the region of the deeper eclipse and residuals.

Table 7
Photometric Orbital Parameters for BF Dra in the *V* Band

Parameter	URSA	NFO	Adopted
J_A/J_B	0.967 ± 0.003	0.982 ± 0.004	0.974 ± 0.006
$r_A + r_B = (R_A+R_B)/a$	0.1351 ± 0.0001	0.1351 ± 0.0002	0.1351 ± 0.0002
$r_A = R_A/a$	0.0704 ± 0.0002	0.0701 ± 0.0002	0.0703 ± 0.0004
$r_B/= R_B/a$	0.0646 ± 0.0002	0.0650 ± 0.0002	0.0648 ± 0.0004
$k = r_A/r_B$	1.090 ± 0.007	1.079 ± 0.008	1.085 ± 0.006
i (deg)	88.41 ± 0.01	88.43 ± 0.02	88.42 ± 0.02
e	0.3839 ± 0.0007	0.3867 ± 0.0006	0.3853 ± 0.0014
ω_A (deg)	273.62 ± 0.01	273.58 ± 0.01	273.60 ± 0.02
u_A (linear)	0.4162 fixed	0.67 ± 0.02	
$u_A{}'$ (nonlinear)	0.2834 fixed		
u_B (linear)	0.4110 fixed	0.67 ± 0.02	
$u_B{}'$ (nonlinear)	0.2866 fixed		
$y_{A=}\ y_B$	0.32 fixed	0.32 fixed	
$q = m_A/m_B$	1.028 fixed	1.028 fixed	
L_A	0.530 ± 0.002	0.529 ± 0.003	0.530 ± 0.004
L_B	0.462 ± 0.003	0.463 ± 0.004	0.462 ± 0.004
$L_B/(L_A+L_B)$	0.872 ± 0.009	0.875 ± 0.009	0.873 ± 0.009
L_3	0.0074 fixed	0.0074 fixed	
σ (mmag)	6.961938	6.207638	
N	7494	9700	
Corrections	113	261	

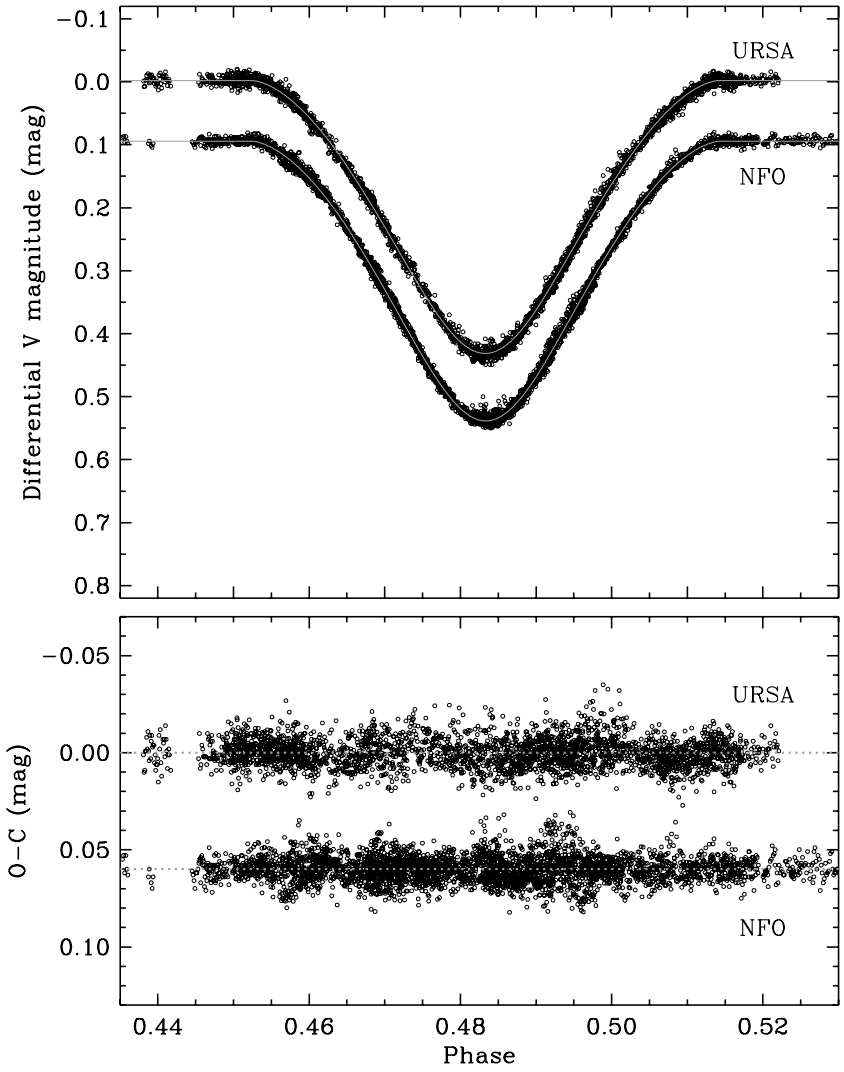

Figure 6. Close-up of the region of the shallower eclipse and residuals.

Lacy (1987) showed that the difference in visual surface brightness parameter, ΔF_v, is related to the normalized V-band central surface brightness of the cooler star in eclipsing binaries: $\Delta F_v = 0.25 \log J_c'$. Here, J_c is a parameter that is fitted in the *jktebop* code that we use to model the light curves. Popper's (1980) Table 1 gives the relationship between the visual surface brightness parameter F_v and the stellar temperature, thus the difference in temperature is readily and very accurately determined from the V-filter light curve fit alone. It is not necessary to have additional light curves in different bandpasses in order to determine accurately the temperature difference if this method is used.

Tests for third light showed that it is present at a significant, though very small, level, and the two photometric data sets did not agree well on the value. Close examination of NFO images does show a faint visual companion located northeast of the binary with an angular separation of 12 arcsec. This visual companion was included in our measurement apertures for both URSA and NFO magnitudes. The brightness ratio between the companion and the eclipsing binary star outside eclipse was carefully measured on 100 well-resolved images to be 0.0075 ± 0.0002. This value implies a luminosity ratio $(L_3/(L_1+L_2+L_3)) =$ 0.0074 ± 0.0002. In analyzing the photometry, the value of "third light" (L_3) was fixed at this level. A search was made for the presence of any additional close companion in the CfA spectra, but none was found.

A number of tests have been made comparing the NDE model used by *jktebop* with more complicated models (Popper & Etzel 1981; North & Zahn 2004) including the WD model. The primary results of these studies are that the limits for high-accuracy determination of parameters such as the radii, inclination, etc., with the NDE model are component oblateness less than 0.04 and mean radii less than 0.25. Since the BF Dra properties are all well within these limits, we do not feel the need to use a more complicated model in this case.

The orbital parameters e and ω have been measured by us in three entirely independent model fits: from radial velocities (Table 2: 0.3865 ± 0.0007 and 273.°64 ± 0.°10), from dates of minima (Table 4: 0.3865 ± 0.0005 and 273.°62 ± 0.°02), and from differential photometry (Table 7: 0.3853 ± 0.0014 and 273.°60 ± 0.°02). In every case, the fitted values agree with each other to within the adopted uncertainties. This gives us some confidence in our methods and results of orbital fitting.

The value of the light ratio L_B/L_A adopted from the photometric orbits does differ slightly from the mean spectroscopically estimated value (see Section 3.4), though the difference is not statistically significant based on the adopted uncertainties, and the photometric value actually has twice the statistical weight

Table 8
Absolute properties of BF Dra

Parameter	Primary[a]	Secondary
Mass (solar masses)	1.414 ± 0.003	1.375 ± 0.003
Radius (solar radii)	2.086 ± 0.012	1.922 ± 0.012
log g (cm s^{-2})	3.950 ± 0.005	4.008 ± 0.005
Eccentricity, e	0.3864 ± 0.0004	
$v \sin i$ (km s^{-1}) (observed value)	10.5 ± 1.8	9.0 ± 1.8
Circular $v_{\rm sync}$ (km s^{-1}) (equatorial)	9.4	8.7
Orbital semi-major axis a (solar radii)	29.664 ± 0.021	
$T_{\rm eff}$ (K)	6360 ± 150	6400 ± 150 K
log L (solar units)	0.81 ± 0.04	0.75 ± 0.04
M_V (mag)	2.67 ± 0.12	2.82 ± 0.11
F_V	3.799 ± 0.012	3.802 ± 0.011
E_{b-y} reddening (mag)	0.019 ± 0.010	
$m - M$ (mag)	7.74 ± 0.16	
Distance (pc)	354 ± 27	

Note. [a] The primary star A is the more massive one, which is larger and cooler than the secondary star.

of the spectroscopic value. If the value of the light ratio is fixed at the spectroscopic mean value, however, and the other photometric elements are allowed to vary to their optimum values, the resultant values of the relative radii, r_A and r_B, do change by +0.7% and −1.1%, respectively. In order to be very conservative in our error estimates, we have decided to double the formal uncertainties in the relative radii to reflect the possible difference between the photometric and spectroscopic light ratios, and the uncertainty in the quadratic limb-darkening values mentioned earlier.

4. ABSOLUTE PROPERTIES AND COMPARISON WITH THEORY

The combination of the spectroscopic results of Table 2 with the light curve results in Table 7 leads to the absolute dimensions and masses for BF Dra shown in Table 8. Table 1 of Popper (1980) has been used for the radiative quantities. We have adopted the value of the eccentricity e as a weighted average of the various determinations discussed above. The masses are determined to an accuracy of 0.3% (standard error), and the radii are good to about 0.6% (standard error). We have conservatively estimated the uncertainties in the effective temperatures to be 150 K (standard error) to include possible systematic errors in the photometry and in the calibrations of Popper (1980).

The distance we derive for the system corresponds to a parallax of $\pi = 2.83 \pm 0.21$ mas. The *Hipparcos* catalog lists the parallax as 1.78 ± 0.98 mas, not significantly different from our result. The revised *Hipparcos* parallax (van Leeuwen 2007) of 2.54 ± 0.97 mas improves the agreement.

The accurate physical dimensions derived for BF Dra allow for a meaningful test of stellar evolution theory. In Figure 7, we compare the observations against the Yonsei–Yale models of Yi et al. (2001), which include convective core overshooting in the amount of $\alpha_{\rm ov} = 0.20\ H_p$, where H_p is the pressure scale height (Demarque et al. 2004).

The mixing length parameter adopted is $a_{\rm ML} = 1.7431$. Evolutionary tracks for the exact masses we measure for each component (solid lines) are shown for the metallicity that best fits the observations, which is $Z = 0.0126$ (corresponding to [Fe/H] = −0.17 in these models, for $Y = 0.255$), assuming [a/Fe] = 0.0, where [a/Fe] measures the a-element enhancement relative to iron. The agreement with the observations is

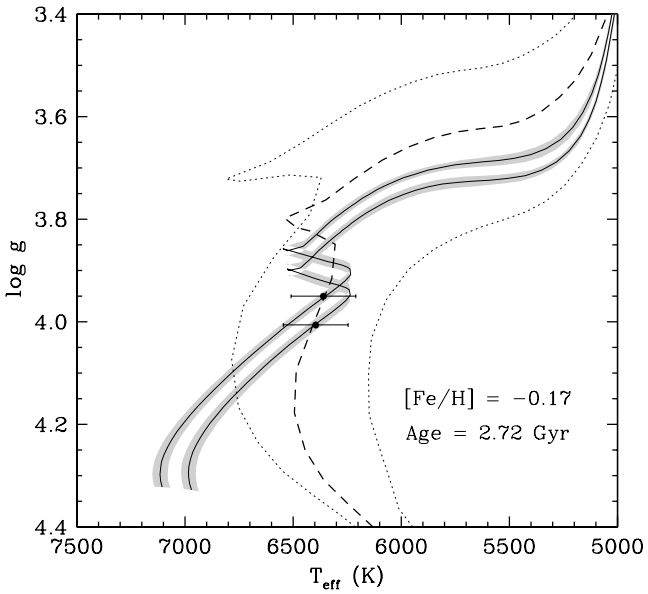

Figure 7. Measurements for BF Dra compared against Yonsei–Yale models by Yi et al. (2001) for [Fe/H] = −0.17 and [α/Fe] = 0.0. The solid lines represent evolutionary tracks for the measured masses, and the shaded areas indicate the uncertainty in the location of each track coming from the mass errors. Isochrones for 2 and 5 Gyr are shown with dotted lines, and the dashed line represents the best-fitting isochrone for an age of 2.72 Gyr.

excellent, including the small difference in temperature between the stars. The Yonsei–Yale calculations suggest an age of 2.72 Gyr for the system; the corresponding isochrone is shown with a dashed line. Both stars are nearing the end of their main-sequence phase. The 150 K uncertainties in the effective temperatures lead to uncertainties in the inferred metallicity and age of BF Dra that we estimate to be 0.10 dex and 0.21 Gyr, respectively.

A similar comparison was carried out with the models of Claret (2004), in which the mixing length parameter calibrated to the Sun is $a_{\rm ML} = 1.68$. When adopting, as before, a convective core overshooting parameter of $a_{\rm ov} = 0.20\ H_{\rm p}$, we find once again an excellent fit with a metallicity of $Z = 0.0135$ (corresponding to [Fe/H] = −0.15 in these models, with $Y = 0.267$) and an age of 2.78 Gyr, very near the values from the previous models. The uncertainties due to the temperature errors are again about 0.10 dex and 0.20 Gyr in metallicity and age. For both sets of models the inferred metallicity is consistent with the less accurate estimate obtained from the Stromgren photometry, [Fe/H] = −0.03 ± 0.15

The stellar evolution calculations above adopt the standard mixing-length approximation for the treatment of convection and similar prescriptions for convective core overshooting. In this framework, the location of the stars in BF Dra near the point of hydrogen exhaustion presents an opportunity to investigate the importance of overshooting, given that the extent of the main sequence toward the right in Figure 7 depends strongly on this parameter. For larger values of $\alpha_{\rm ov}$ the main-sequence phase reaches cooler temperatures and lower surface gravities. Using the models of Claret (2004), we calculated evolutionary tracks for the best-fit metallicity of [Fe/H] = −0.15 and values of $\alpha_{\rm ov} = 0.00$ to $0.20\ H_p$, in steps of $0.05\ H_p$. Each pair of tracks is compared with the observations in Figure 8. Overshooting parameters lower than about $0.13\ H_p$ do not provide a good fit to the measured mass, radius, and temperature of one or both stars. We conclude that the measurements of BF Dra provide a useful lower limit to overshooting for stars near 1.4 solar

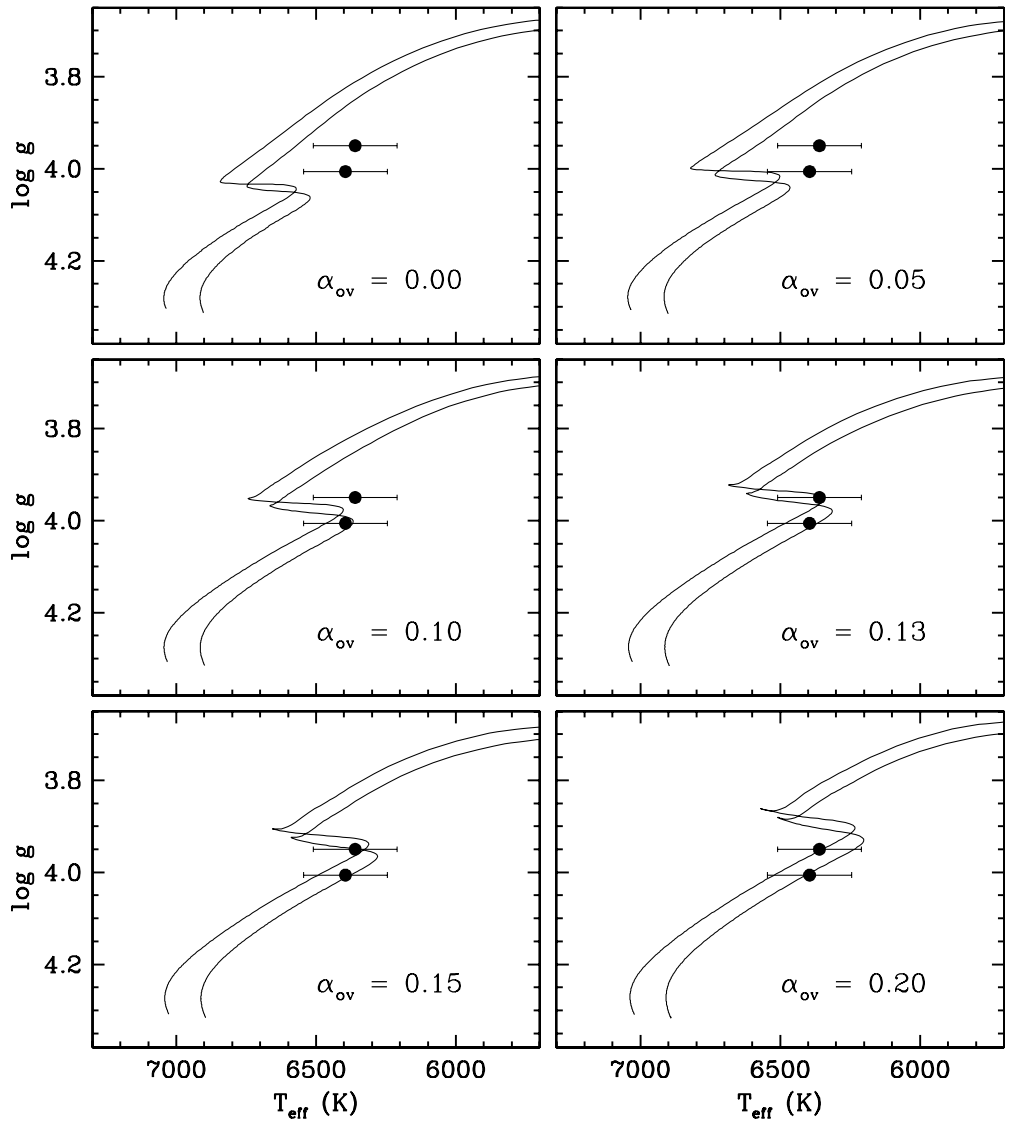

Figure 8. Measurements for BF Dra compared against evolutionary tracks from Claret (2004) for the measured masses, calculated for a range of convective core overshooting parameters α_{ov}, as labeled. All tracks are computed for a metallicity of [Fe/H] = −0.15 and [α/Fe] = 0.0 (see the text).

masses, demonstrating that a non-zero value is needed to match the observational results.

4.1. Comparison with Tidal Evolution Theory

On the assumption that the spin axes of the BF Dra components are parallel to the orbital axis, the measured projected rotational velocities are consistent with the values expected if tidal forces had synchronized the stars to the orbital motion for a circular orbit with the measured period. However, the orbit has a significant eccentricity of $e = 0.3864$, and the pseudo-synchronous rotation rate at which the components are eventually expected to settle (Hut 1981) is considerably higher than measured (see Table 8). Similar problems of non-synchronized stars have been reported previously for a number of other binary systems such as V364 Lac (Torres et al. 1999), V459 Cas (Lacy et al. 2004), RW Lac (Lacy et al. 2005), AS Cam (Pavlovski et al. 2011), and many others. Misalignment of the spin and orbital axes is one possible explanation, as has been beautifully demonstrated for DI Her by Albrecht et al. (2009) in connection with the decades-old mystery of its anomalously slow apsidal motion. A similar connection between slow apsidal motion and misaligned spin axes is postulated for AS Cam (Pavlovski et al. 2011). Here we investigate in more detail the predictions of tidal theory for the circularization of the orbit of BF Dra, the synchronization of the rotation rates, as well as the alignment of the spin axes of the stars relative to the orbital axis. For an overview on all of these issues we refer the reader to the review article by Mazeh (2008).

We follow closely the procedure of Torres et al. (2012), and perform numerical integrations of the equations that govern the evolution of the semimajor axis, the eccentricity, the inclination angles between the star's equators and the orbital plane, and the angular rotation rates of the components, as described by Hut (1981). The six coupled differential equations (da/dt, de/dt, $d(\phi_1)/dt$, $d(\phi_2)/dt$, $d(\Omega_1)/dt$, $d(\Omega_2)/dt$) are integrated simultaneously using a fourth-order Runge–Kutta method, with stellar properties at each time step taken from the same evolutionary tracks used above based the stellar evolution models by Claret (2004), for $Z = 0.0135$ and $\alpha_{ov} = 0.20$. Changes in metallicity of the order of the uncertainties reported in the previous section ($\pm$ 0.10 dex in [Fe/H]) have a negligible impact on these calculations, and on the conclusions drawn below.

The initial conditions of the problem are not known, so they are free parameters of our model. For the orbital period and

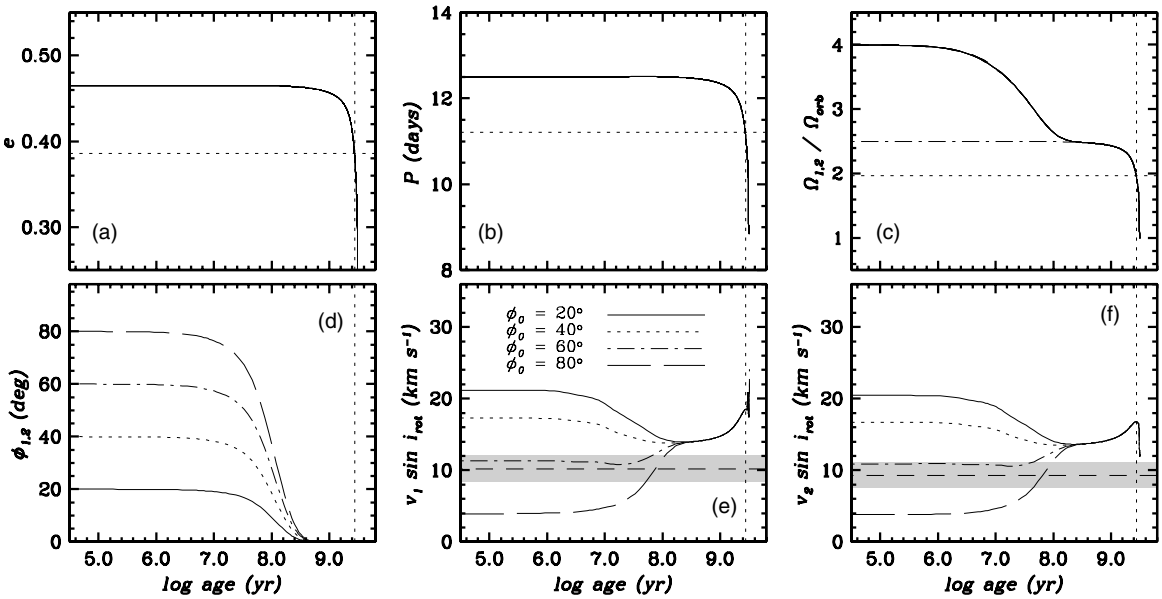

Figure 9. Tidal evolution calculations for BF Dra following the prescription by Hut (1981). The vertical dotted line in each panel represents the current evolutionary age of 2.78 Gyr (log age = 9.44), based on the models by Claret (2004; see the text). Results are shown only for the primary (more massive star), as the curves for the secondary are virtually indistinguishable on account of their similar mass. These calculations assume an initial rotation rate for both stars of $\Omega/\Omega_{orb} = 4$. (a) Eccentricity as a function of time (current value indicated by the horizontal dotted line); (b) orbital period (current value indicated by the horizontal dotted line); (c) normalized angular rotation rate of each star. The dot-dashed line represents the evolution of the pseudo-synchronous value, and the horizontal dotted line is the pseudo-synchronous rate at the present age. (d) Angle between the equator of each star and the plane of the orbit. The four curves correspond to different initial values as labeled in the next panel. (e) Theoretical projected rotational velocity of the primary star as a function of time, for four values of the initial spin–orbit angle ϕ_0. The measured $v \sin i_{rot}$ and its uncertainty are indicated with the horizontal dashed line and shaded area, and disagree with theory. (f) Same as (e) for the secondary.

eccentricity we find that initial values of approximately $P_0 = 12.5$ days and $e_0 = 0.465$ enable us to match the present-day values of $P = 11.211$ days and $e = 0.3864$ at the current evolutionary age of the system (2.78 Gyr in these models, or log age = 9.44). The time evolution of the period and eccentricity are shown in Figures 9(a) and (b). Based on these calculations, circularization of the orbit is expected to occur at an age of about 3.2 Gyr (log age = 9.50).

The evolution of the angular rotation rate $\Omega = 2^*\pi/P_{rot}$ is seen in Figure 9(c) for the primary (more massive) star, where for convenience we have normalized it to the orbital rate, $\Omega_{orb} = 2^*\pi/P_{orb}$. The curve for the secondary is nearly identical and is not shown. There is no observational constraint on the rotation rates, so we have taken arbitrary initial values of $\Omega_1/\Omega_{orb} = \Omega_2/\Omega_{orb} = 4$. The impact of this assumption is explored below. The dot-dashed line in this panel represents the pseudo-synchronous rate at each age, and the models predict that this rate would have been reached when the system was only 270 Myr old (log age = 8.43), which is one-tenth of its present age. The observations contradict this, as indicated earlier.

It is possible, in principle, that the slow $v \sin i$ values we measure are the result of misalignment of the spin axes relative to the orbital axis, with a projection factor to the line of sight that could then be considerably smaller than unity. However, once again we have no observational constraint on the misalignment angle ϕ, nor can it usually be measured directly. This is because the relation between ϕ and the orbital and rotational inclination angles i_{orb} and i_{rot}, both of which are measured with respect to the line of sight, is given by

$$\cos\phi = \cos i_{orb}{}^* \cos i_{rot} + \sin i_{orb}{}^* \sin i_{rot}{}^* \cos\lambda, \qquad (1)$$

which not only involves the angle i_{rot} that is generally inaccessible to observation, but it also involves the unknown angle λ between the sky-projected angular momentum vectors of the orbit and the stellar spin.

While the spectroscopically measured projected rotational velocities of the stars (which we refer to more properly now as $v \sin i_{rot}$) do provide an indirect constraint on a combination of theoretically predictable quantities, this still involves the unknown angle lambda.[8] Given that i_{orb} is within 2° of edge-on, we make the approximation here that $\cos\phi \sim \sin i_{rot}{}^* \cos\lambda$, which leads to

$$v \sin i_{rot} \sim [2^*\pi/P_{orb}][\Omega/\Omega_{orb}][\cos\phi/\cos\lambda]R. \qquad (2)$$

The quantities on the right-hand side of this equation are either known from stellar evolution calculations (e.g., R) or can be computed from the solution of the differential equations for tidal evolution. The exception is the angle λ, which depends on the observer's vantage point. We will assume for the moment that λ is small, which allows us to proceed by ignoring the cos λ term in Equation (1) so that $\cos\phi \sim \sin i_{rot}$.

The resulting evolution of the alignment angle ϕ for BF Dra is displayed in Figure 9(d) for four different initial spin–orbit angles (20°, 40°, 60°, and 80°). Only the curves for the primary are shown, as they are indistinguishable from those of the secondary. The convergence of the curves at an age of about 500 Myr (log age = 8.7, or one-fifth of the present age) indicates that spin–orbit alignment is reached early on in the system, independently of the initial value of ϕ. Thus, theory seems to exclude the possibility that the disagreement between the measured and predicted rotational velocities is due to misalignment of the spin axes. The predicted evolution of $v \sin i_{rot}$ for each star, as computed from Equation (2), is shown

[8] This angle can be measured in favorable cases through the Rossiter–McLaughlin effect (see, e.g., Albrecht et al. 2009; Albrecht 2011), although such measurements are not available for BF Dra.

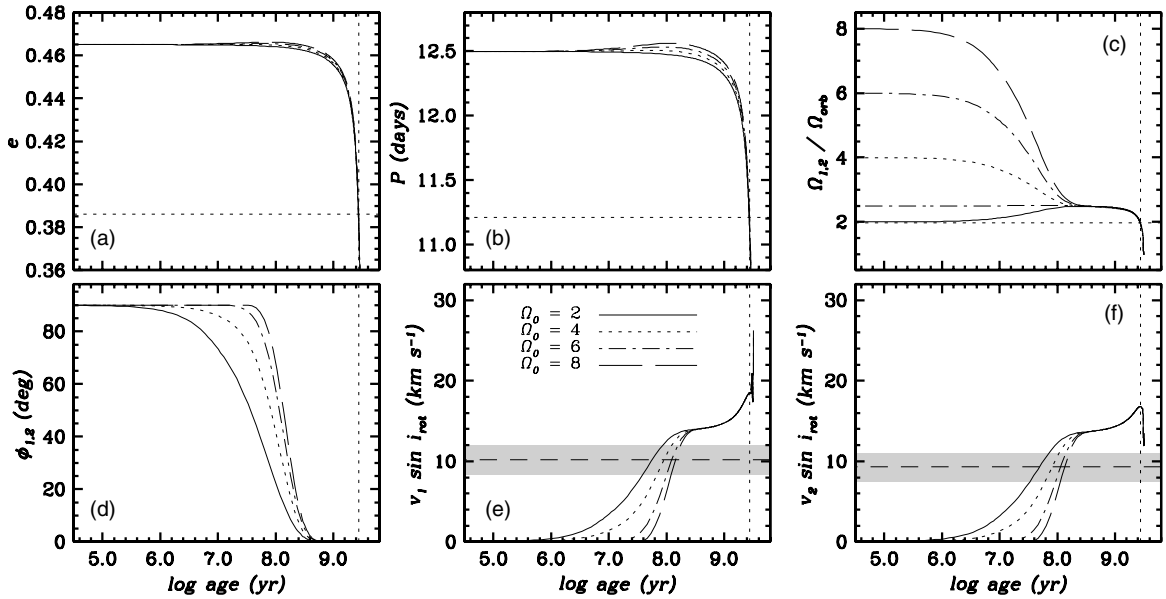

Figure 10. Similar to Figure 9, where instead of varying the initial spin–orbit angle we have tested four different values of the initial normalized rotation rates of the stars, as labeled in panel (e). The initial value of the spin–orbit angle is set to 90°.

in Figures 6(e) and (f). The measured values (10.5 ± 1.8 km s^{-1} and 9.0 ± 1.8 km s^{-1} for the more massive and less massive stars, respectively) are indicated with the dashed lines and shaded uncertainty intervals.

The incidence of the initial value of the rotation rate Ω on the evolution of the various quantities influenced by tidal effects is illustrated in Figure 10. The panels are the same as in Figure 9, but instead of varying ϕ_o, we fix ϕ_o to 90° and we set Ω_0 to values of 2, 4, 6, and 8. The result that both components seem to be rotating sub-synchronously by nearly a factor of two is unchanged.

We conclude that while current tidal evolution theory correctly predicts that the orbit of BF Dra should not yet have circularized, these models are unable to match the anomalously slow rotation rates measured for the two components. We note also that our assumption above that the angle λ is small has no impact on this latter conclusion, as any value greater than zero only makes the disagreement worse (increasing the predicted rotational velocities). A possible explanation for this behavior of $v \sin i_{\rm rot}$, mentioned also by other authors, is the idea of decoupling between the core of the star and the surface layers, which may be rotating at different rates. Our models assume rigid body rotation, so that the predictions from tidal theory may be more representative of a more rapidly rotating core than of the outer envelope, or at the very least some average of the two, which would be larger than the measured value.

4.2. Internal Structure

The detection of apsidal motion in BF Dra, $d\omega/dt = 1.^\circ60 \pm 0.^\circ26$ century^{-1}, along with our precise measurement of the absolute dimensions, enables an interesting test of the predictions of interior structure models. The relativistic contribution to the apsidal motion in this system is very significant (51%). Removing this component after Gimenez (1985) yields a net Newtonian motion of $(d\omega/dt)_{\rm Newt} = 0.^\circ79 \pm 0.^\circ06$ century^{-1}, from which we infer an average internal structure constant of $\log k_2({\rm obs}) = -2.28 \pm 0.13$. Using the same Claret (2004) models as above for $\alpha_{\rm ov} = 0.20$, we derive a weighted mean theoretical value of the two components of $\log k_2({\rm theo}) = -2.40 \pm 0.05$. Thus, theory and observation agree, within the errors, regarding the average degree of mass concentration of the stars.

The authors thank Bill Neely who operates and maintains the NFO WebScope for the Consortium, and who handles preliminary processing of the images and their distribution. The authors also thank the staff at KPNO, especially Daryl Willmarth, for maintenance and preparation of the coudé-feed telescope and spectrometer. G.T. acknowledges partial support from the NSF grant AST-10-07992. Thanks also to University of Arkansas graduate student Mythra Varun Nemallapudi for initial analysis of the URSA photometry and preliminary radial velocities.

REFERENCES

Agerer, F., & Hübscher, J. 1998, IBVS, 4606
Albrecht, S. 2011, in IAU Symp. 282, in press (arXiv:1109.1750)
Albrecht, S., Reffert, S., Snellen, I. A. G., & Winn, J. N. 2009, Nature, 461, 373
Alonso, A., Arribas, S., & Martínez-Roger, C. 1996, A&A, 313, 873
Brát, L., Zejda, M., & Svoboda, P. 2007, Open Eur. J. Variable Stars, 74
Caton, D. B., & Smith, A. B. 2005, IBVS, 5595
Claret, A. 1998, A&AS, 131, 395
Claret, A. 2000, A&A, 363, 1081
Claret, A. 2004, A&A, 424, 919
Claret, A., & Hauschildt, P. H. 2003, A&A, 412, 241
Crawford, D. L., & Barnes, J. V. 1974, AJ, 79, 687
Demarque, P., Woo, J., Kim, Y., & Yi, S. K. 2004, ApJS, 155, 667
Diaz-Cordoves, J., Claret, A., & Gimenez, A. 1995, A&AS, 110, 329
Diethelm, R. 1993, BBSAG Bull., No. 103
Diethelm, R. 1996, BBSAG Bull., No. 111
Diethelm, R. 2001, BBSAG Bull., No. 126
Diethelm, R., Wolf, M., & Agerer, F. 1993, IBVS, 3867
Doppner, M. 1962, MVS (Sonneberg), No. 699
Eaton, J. A., & Williamson, M. H. 2007, PASP, 119, 886
Etzel, P. B. 1981, in Photometric and Spectroscopic Binary Systems, ed. C. B. Carling & E. Z. Kopal (Dordrecht: Reidel), 111
Fekel, F. C. 1997, PASP, 109, 514
Fekel, F. C., Tomkin, J., & Williamson, M. H. 2009, AJ, 137, 3900
Furesz, G. 2008, PhD thesis, Univ. Szeged, Hungary
Gimenez, A. 1985, ApJ, 297, 405
Grauer, A. D., Neely, A. W., & Lacy, C. H. S. 2008, PASP, 120, 992
Hayes, D. S. 1978, in IAU Symp. 80, The HR Diagram, ed. A. G. D. Philip & D. S. Hayes (Dordrecht: Reidel), 65

Hübscher, J. 1992, BAV Mitt., No. 60
Hübscher, J., Lehmann, P. B., Monninger, G., Steinbach, H., & Walter, F. 2010a, IBVS, 5918
Hübscher, J., Lehmann, P. B., Monninger, G., Steinbach, H., & Walter, F. 2010b, IBVS, 5941
Hübscher, J., Steinbach, H., & Walter, F. 2008, IBVS, 5830
Hut, P. 1981, A&A, 99, 126
Imbert, M. 1985, A&AS, 59, 357
Lacy, C. H. S. 1987, AJ, 94, 1035
Lacy, C. H. S. 1992, AJ, 104, 2213
Lacy, C. H. S. 2002, AJ, 124, 1162
Lacy, C. H. S. 2006, IBVS, 5670
Lacy, C. H. S. 2007, IBVS, 5764
Lacy, C. H. S. 2009, IBVS, 5910
Lacy, C. H. S. 2011, IBVS, 5972
Lacy, C. H. S., Claret, A., & Sabby, J. A. 2004, AJ, 128, 1340
Lacy, C. H. S., Torres, G., Claret, A., & Vaz, L. P. R. 2005, AJ, 130, 2838
Latham, D. W. 1992, in ASP Conf. Ser., Vol. 32, IAU Coll. 135, Complementary Approaches to Double and Multiple Star Research, ed. H. A. McAlister & W. I. Hartkopf (San Francisco, CA: ASP), 110
Locher, K. 1980, BBSAG Bull., No. 50
Locher, K. 1988, BBSAG Bull., No. 88
Mazeh, T. 2008, in Tidal Effects in Stars, Planets and Disks, ed. M.-J. Goupil & J.-P. Zahn (EAS Publ. Ser. 29, Cambridge: Cambridge Univ. Press), 1
North, P., & Zahn, J.-P. 2004, New Astron. Rev., 48, 741
Paschke, A. 1989, BBSAG Bull., No. 92
Pavlovski, K., Southworth, J., & Kolbas, V. 2011, ApJ, 734, L29
Perry, C. L., & Johnson, L. 1982, ApJS, 50, 451
Popper, D. M. 1980, ARA&A, 18, 115
Popper, D. M., & Etzel, P. B. 1981, AJ, 86, 102
Scarfe, C. D. 2010, Observatory, 130, 214
Selman, F. J. 2004, Proc. SPIE, 5493, 453
Smith, A. B., & Caton, D. B. 2007, IBVS, 5745
Southworth, J., Bruntt, H., & Buzasi, D. L. 2007, A&A, 467, 1215
Strohmeier, W., Knigge, R., & Ott, H. 1962, Veröff. Remeis-Stern. Bamberg, Band V, No. 14
Strohmeier, W., Knigge, R., & Ott, H. 1963, Veröff. Remeis-Stern. Bamberg, Band V, No. 16
Stromgren, B. 1966, ARA&A, 4, 433
Tomkin, J., & Fekel, F. C. 2006, AJ, 131, 2652
Torres, G., Andersen, J., & Giménez, A. 2010, A&AR, 18, 67
Torres, G., Clausen, J. V., Bruntt, H., et al. 2012, A&A, 537, A117
Torres, G., Lacy, C. H. S., Claret, A., et al. 1999, AJ, 118, 1831
van Leeuwen, F 2007, Hipparcos, The New Reduction of the Raw Data (Astronomy & Space Science Library; Dordrecht: Springer), 350
Wolf, M., Claret, A., Kotkova, L., et al. 2010, A&A, 509, A18
Yi, S. K., Demarque, P., Kim, Y.-C., et al. 2001, ApJS, 136, 417
Zucker, S., & Mazeh, T. 1994, ApJ, 420, 806